engineering proceedings

MDPI

Proceeding Paper

Position Sensor Fault-Tolerant Control of IPMSM Drives Using Hybrid Sensorless Estimation over the Full Speed Range †

Berkay Sipahi * and Fikret Caliskan

Department of Control and Automation Engineering, Istanbul Technical University, Istanbul 34467, Turkey; caliskanf@itu.edu.tr

* Correspondence: sipahi17@itu.edu.tr

† Presented at the 13th International Electronic Conference on Sensors and Applications, 18–20 November 2026; Available online: https://sciforum.net/event/ECSA-13.

Abstract

This study proposes a new hybrid sensorless control estimation structure that provides a fault-tolerant control (FTC) when a position sensor fault occurs in a permanent magnet synchronous motor (PMSM). The proposed hybrid estimator combines two techniques using a speed-dependent weighting transition. High-frequency signal injection is applied at standstill and low speeds, while an extended Back-EMF observer takes over the position estimation at higher speeds. Within the transition band, the two estimators are combined by a vectorial cross-fade, resulting in a continuous position estimate. The sensor fault is detected by monitoring the angular difference between the sensor output and the complementary sensorless estimation output. The residual threshold is adjusted dynamically so that false triggers and missing triggers are avoided during acceleration and deceleration. Additionally, a decision-making delay is added to prevent noise-induced false alarms. When the fault is detected, the position feedback is smoothly switched to hybrid sensorless operation without interruption. The proposed strategy is tested across the full speed range of the PMSM via simulation, including steady-state, transient, and both fault-free and sensor fault scenarios. As a result of these scenarios, a new hybrid sensorless estimation structure capable of handling low-amplitude sensor biases in the position sensor across the full speed range is designed. Also, the Back-EMF estimation is compared with the extended Kalman filter at medium and high speeds, demonstrating a lower error detection threshold, quicker response, and reduced computational load.

Keywords: PMSM; fault-tolerant control; position sensor fault; sensorless control; high-frequency signal injection; extended Back-EMF observer; weighted transition

Check for updates

Academic Editor: Stefano Mariani

Published: 27 October 2026

Copyright: © 2026 by the authors. Licensee MDPI, Basel, Switzerland. This article is an open access article distributed under the terms and conditions of the Creative Commons Attribution (CC BY) license.

1. Introduction

Interior permanent magnet synchronous motors (IPMSMs) are widely used in electric vehicle traction and industrial servo drives due to their high torque density and wide constant power region. Field-oriented control (FOC) of these machines requires continuous rotor position feedback, which is generally provided by a resolver or encoder. Sensor faults and failures such as complete loss of signal, intermittent loss or measurement error can disrupt the *d*-*q* decoupling and cause uncontrolled torque responses. Therefore, fault-tolerant control (FTC) strategies that detect faults and reconfigure the drive to sensorless operation are commonly used in safety-critical drive designs [1,2].

Sensorless position estimation methods depend on operating speed. At medium and high speeds, Back-Electromotive Force (Back-EMF)-based observers estimate the rotor angle

from induced voltage. An extended Back-EMF model is used to design a simple disturbance observer for salient-pole permanent magnet synchronous motors (PMSMs) without model approximations [3]. However, these approaches fail at low and zero speeds because the Back-EMF magnitude becomes very small when the motor is near standstill. At these speeds, high-frequency (HF) signal injection techniques fill this gap by using magnetic saliency ($L_d \neq L_q$) of the IPMSM [4]. A superimposed carrier voltage in high-frequency signal injection (HFSI) causes a position dependent current response and rotor angle is demodulated from this response. Pulsating injection offers higher accuracy and lower sensitivity to inverter dead-time effects than rotating injection [5]. Since neither technique alone covers full speed range, a transition mechanism is needed for continuous sensorless operation over the full speed range [6].

Two transition strategies have been reported in the literature: hysteresis-based hard switching and weighting-based soft transition. Hysteresis-based switching is computationally simple, but it causes torque and speed ripples at transition point, because two estimators produce different outputs at switching instant. On the other hand, the weighting-based transition eliminates these discontinuities by combining both estimates within speed band. This implementation reduces injection loop gain linearly to zero during the transition region [6]. In this paper, a vectorial cross-fade has been used based on sin/cos decomposition. This method also eliminates 2π wrapping effects that exist in direct angle combinations.

For fault detection, a commonly used approach in the literature monitors the deviation between the sensor angle and a sensorless estimation. The reconfiguration is triggered when this difference exceeds a threshold value [1]. A fixed threshold should be greater than worst case transient overshoot during acceleration and deceleration. This limitation causes slower detection and increases the duration of the current disturbance [7]. This trade-off is improved by adaptive threshold designs based on phase-locked loop (PLL) estimation dynamics and cumulative sum (CUSUM) algorithm [8]. However, current implementations do not cover standstill or low speeds because they mostly depend on Back-EMF estimates [9]. Statistical alternatives to geometric thresholding have also been explored, including sequential hypothesis testing [10], Mahalanobis-distance-based observation weighting [11], and residual-duration dual-parameter diagnosis for Kalman-filter-based position sensor fault detection [12].

This paper proposes a hybrid FTC architecture that performs fault detection across the entire speed range with dynamic threshold. The main contributions are as follows:

1. A hybrid sensorless estimator that runs HF pulsating injection at standstill and low speeds and an extended Back-EMF disturbance observer at medium and high speeds in the background of the sensor based FOC. This estimator provides full speed range diagnostic.
2. A vectorial weighted transition that combines two estimations within transition band by using sin/cos decomposition. This transition provides a smooth combined position information without wrapping.
3. The residual signal is determined based on the difference between the position information from sensor and estimation from sensorless methods. Thanks to the on-delay and dynamic threshold, false alarms are prevented.
4. A smooth reconfiguration is ensured, when a fault is detected. Estimation methods always run in the background for this bumpless reconfiguration.

The proposed strategy is validated on a MATLAB/Simulink (version R2023a; The MathWorks Inc., Natick, MA, USA) model of an IPMSM drive. The remainder of this paper is organized as follows. Section 2 presents the IPMSM model. Section 3 explains the hybrid estimation and transition algorithm. Section 4 describes the fault detection and

reconfiguration logic. Section 5 presents the simulation results, and Section 6 concludes the paper.

2. Mathematical Model of the IPMSM

The IPMSM model used throughout this work is formulated in the rotor reference frame and then transformed into the estimated synchronous frame to support the Back-EMF observer. The model has been limited to the fundamental electrical behaviour relevant to position estimation and fault detection, cogging torque, iron losses, and magnetic saturation have been neglected.

2.1. Voltage Equations in the Rotor Reference Frame

Applying the Park transformation to three phase stator voltage equations yields the IPMSM model in rotor aligned *d*-*q* frame

$$\begin{aligned} v_d &= R_s i_d + L_d \frac{di_d}{dt} - \omega_e L_q i_q, \\ v_q &= R_s i_q + L_q \frac{di_q}{dt} + \omega_e (L_d i_d + \psi_m), \end{aligned} \tag{1}$$

where v_d, v_q and i_d, i_q are the *d*- and *q*-axis stator voltages and currents, R_s is the stator resistance, L_d and L_q are the *d*- and *q*-axis inductances, ψ_m is the permanent magnet flux linkage, and $\omega_e = p\,\omega_m$ is the electrical angular velocity, with p the number of pole pairs and ω_m the mechanical angular velocity. For an IPMSM the inductances satisfy $L_q > L_d$, this magnetic saliency has been used on HF injection method introduced in Section 3.1.

2.2. Extended Back-EMF Formulation

The model (1) cannot be applied directly in a sensorless drive because the *d*-*q* frame is defined by the unknown rotor angle θ_e. The geometric relations between relevant reference frames have been summarized in Figure 1. Transforming (1) into the estimated synchronous frame γ-δ, whose orientation differs from *d*-*q* by the estimation error $\Delta\theta = \theta_e - \hat{\theta}_e$, does not by itself resolve the difficulty. When $L_d \neq L_q$, the rotor frame inductance matrix diag(L_d, L_q) is not invariant under this change of basis, and the transformed model contains non-diagonal terms that directly depend on $\Delta\theta$.

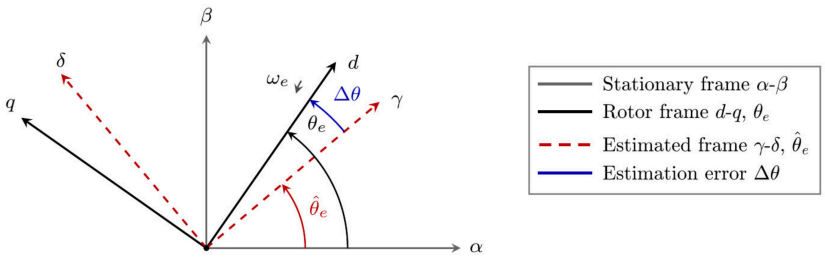


Figure 1. Reference frames: stationary α-β, rotating *d*-*q* and estimated γ-δ.

The extended Back-EMF formulation [3,13] eliminates this coupling by an algebraic rearrangement of (1). That absorbs all saliency-related effects into a single *q*-axis voltage source while providing inductance matrix free of speed-dependent terms. After performing the required substitutions and simplification, the IPMSM model takes the compact matrix form

$$\begin{bmatrix} v_d \\ v_q \end{bmatrix} = \begin{bmatrix} R_s + sL_d & -\omega_e L_q \\ \omega_e L_q & R_s + sL_d \end{bmatrix} \begin{bmatrix} i_d \\ i_q \end{bmatrix} + \begin{bmatrix} 0 \\ E_{ex} \end{bmatrix}, \tag{2}$$

where $s \triangleq d/dt$ and the extended Back-EMF is defined as

$$E_{ex} = \omega_e \left[\left(L_d - L_q \right) i_d + \psi_m \right] - \left(L_d - L_q \right) \frac{di_q}{dt}. \tag{3}$$

Two properties of (2) underpin the observer design. The inductance appears in impedance matrix as sL_d, that is independent of speed. Also, all rotor position information has been included in the single voltage vector $[0,\ E_{ex}]^\top$ aligned with q-axis. Because of these two features, Equation (2) keeps the same form in any synchronous frame. Sensorless estimation therefore reduces to finding the direction of this voltage vector.

Expression (3) also exposes the principal limitation of Back-EMF. Since each term in E_{ex} is proportional to ω_e or di_q/dt, the rotor angle becomes unobservable during steady-state operation at standstill because the signal vanishes.

To express the model in the estimated frame, the rotation matrix

$$\mathbf{R}(\Delta\theta) = \begin{bmatrix} \cos\Delta\theta & -\sin\Delta\theta \\ \sin\Delta\theta & -\cos\Delta\theta \end{bmatrix} \tag{4}$$

is applied to the voltage and current vectors of (2) to perform the change of reference frame from d-q to γ-δ. Because the impedance matrix is independent of speed, it does not change form in the estimated frame and only the E_{ex} vector is rotated. Evaluating $\mathbf{R}(\Delta\theta)[0,\ E_{ex}]^\top$ yields the scalar projections

$$\begin{aligned} e_\gamma &= -E_{ex}\sin(\Delta\theta), \\ e_\delta &= -E_{ex}\cos(\Delta\theta). \end{aligned} \tag{5}$$

For small estimation errors $\sin(\Delta\theta) \approx \Delta\theta$, so e_γ behaves like linear function of the angular error with slope $-E_{ex}$ close to $\Delta\theta \approx 0$. The Back-EMF observer described in Section 3.2 exploits this property by driving e_γ to zero through a PLL, when $\hat{\theta}_e$ has converged to θ_e.

2.3. Mechanical Dynamics and Electromagnetic Torque

The electromagnetic torque of the IPMSM combines magnet alignment term and a reluctance term caused by saliency

$$T_e = \frac{3}{2}\,p\left[\psi_m i_q + \left(L_d - L_q\right) i_d i_q\right]. \tag{6}$$

The first term in (6) is conventional magnet torque, while the second is the reluctance torque exploited under maximum torque per ampere operation. The mechanical subsystem is defined by Newton's equation

$$J\,\frac{d\omega_m}{dt} = T_e - T_L - B\,\omega_m, \tag{7}$$

together with the kinematic relation $d\theta_m/dt = \omega_m$, where J is rotor moment of inertia, B is viscous friction coefficient, and T_L is external load torque. The electrical position and speed are related to the mechanical quantities through $\theta_e = p\,\theta_m$ and $\omega_e = p\,\omega_m$.

Equations (1)–(7), together with inverter and field-oriented current loop, build architecture where the hybrid sensorless estimator (Section 3) and the fault detection logic (Section 4) operate.

3. Hybrid Sensorless Position Estimation

3.1. High-Frequency Pulsating Signal Injection at Zero and Low Speeds

Since E_{ex} becomes zero near standstill, the HF pulsating signal injection method [4,5] is combined in this structure to restore position observability. It superimposes a high-frequency carrier voltage on the estimated d-axis of the controller and extracts rotor position from the carrier frequency current response, which is modulated by the magnetic saliency $L_d \neq L_q$ of the IPMSM.

https://doi.org/10.3390/engproc2026163015

A pulsating carrier $v_{\hat{d}h} = V_h \cos(\omega_h t)$ is added to the estimated d-axis voltage reference at angular frequency ω_h well above current loop bandwidth. Because the injection is defined in the γ-δ frame, its projection onto actual rotor frame is obtained through $\mathbf{R}^\top(\Delta\theta)$, giving

$$\begin{bmatrix} v^r_{dh} \\ v^r_{qh} \end{bmatrix} = V_h \cos(\omega_h t) \begin{bmatrix} -\cos\Delta\theta \\ -\sin\Delta\theta \end{bmatrix}. \tag{8}$$

Although pulsating carrier signal is only injected on the estimated d-axis, when $\Delta\theta \neq 0$ the same physical voltage vector projects onto both axes through $\cos\Delta\theta$ and $-\sin\Delta\theta$. This q-axis projection, that becomes zero with perfect alignment, makes estimation error observable thanks to saliency $L_d \neq L_q$.

At ω_h, the resistive and rotational terms in (1) are negligible when compared with inductive impedances $j\omega_h L_d$ and $j\omega_h L_q$. Therefore, rotor carrier currents follow from term-by-term integration

$$\begin{bmatrix} i^r_{dh} \\ i^r_{qh} \end{bmatrix} \approx \frac{V_h \sin(\omega_h t)}{\omega_h} \begin{bmatrix} -\cos\Delta\theta/L_d \\ -\sin\Delta\theta/L_q \end{bmatrix}. \tag{9}$$

Transforming (9) back to estimated frame with $\mathbf{R}(\Delta\theta)$ and applying the identity $\sin\Delta\theta\cos\Delta\theta = 1/2\sin(2\Delta\theta)$, the carrier frequency component of the current on the estimated q-axis is

$$i_{qh} \approx \frac{V_h \left(L_q - L_d\right)}{2\,\omega_h L_d L_q} \sin(\omega_h t)\, \sin(2\Delta\theta), \tag{10}$$

which carries the estimation error with saliency dependent term $(L_q - L_d)/(L_d L_q)$. Critically, (10) is independent of ω_e, so the response continues at standstill.

The position information is extracted from (10) in three steps. A second order bandpass filter centred at ω_h with bandwidth B_w

$$H_{BP}(s) = \frac{B_w s}{s^2 + B_w s + \omega_h^2}, \tag{11}$$

isolates the carrier frequency component of i_q from fundamental drive currents. Multiplying bandpass output by the synchronization signal $\sin(\omega_h t)$ and applying $\sin^2(\omega_h t) = 1/2[1 - \cos(2\omega_h t)]$ yields

$$i_{qh} \sin(\omega_h t) = \frac{V_h \left(L_q - L_d\right)}{4\,\omega_h L_d L_q} [1 - \cos(2\omega_h t)] \sin(2\Delta\theta), \tag{12}$$

in which the position information is shifted to baseband, while the modulation simultaneously generates a high-frequency image at $2\omega_h$. A first-order low-pass filter (LPF) with cutoff $\omega_{LP} \ll 2\omega_h$,

$$H_{LP}(s) = \frac{\omega_{LP}}{s + \omega_{LP}}, \tag{13}$$

suppresses the high-frequency image, leaving baseband error signal

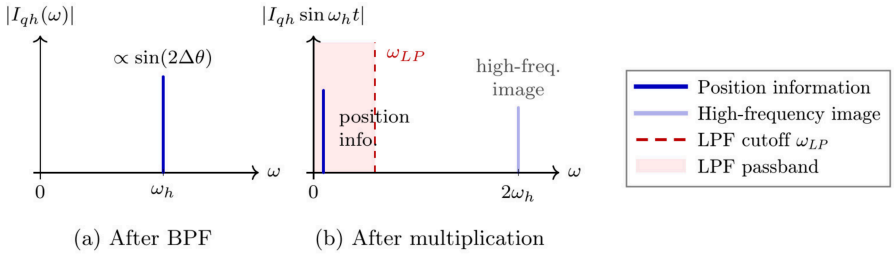
$$\varepsilon_{hf} = K_{hf} \sin(2\Delta\theta) \approx 2K_{hf}\Delta\theta, \tag{14}$$

where the demodulation gain is

$$K_{hf} = \frac{V_h \left(L_q - L_d\right)}{4\,\omega_h L_d L_q}. \tag{15}$$

The error signal ε_{hf} behaves like linear function of the angular error while $\Delta\theta \approx 0$. The progression of the position-bearing content through this chain is shown in Figure 2. After the bandpass filter, position information is centralized at ω_h with amplitude proportional to $\sin(2\Delta\theta)$. Then as a result of multiplication operation, position information carrier signal

and high-frequency image at $2\omega_h$ are formed. Lastly, this high-frequency image signal is filtered with LPF to obtain only position information signal, and the error signal is derived from the remaining component. The distinctive feature of pulsating injection is that position information appears as amplitude of carrier signal and is recovered after demodulation. In rotating signal injection, by contrast, the position information appears at phase of carrier signal rather than amplitude, requiring a different demodulation structure.



(a) After BPF (b) After multiplication

Figure 2. Pulsating injection demodulation: (**a**) bandpass output and (**b**) multiplication by $\sin(\omega_h t)$.

A type-2 PLL is used to get ε_{hf}, a proportional–integral (PI) controller in this PLL drives it to zero and output of controller yields the speed estimate $\hat{\omega}_e^{hf}$. Then that speed is also integrated to obtain the angle estimate $\hat{\theta}_e^{hf}$. In order to clearly separate the angle dynamics from carrier residuals, the PI bandwidth is set well below ω_{LP}.

The reliability of the injection-based estimator degrades at higher speeds because inverter dead-time and switching effects attenuate the carrier signal. Furthermore, as speed increases, the fundamental current frequency approaches to injection frequency, degrading signal quality and demodulation. These effects set an upper bound on the speed at which the HF estimate is reliable.

3.2. Extended Back-EMF Observer at Medium and High Speeds

In this section, Back-EMF observer operates directly on the rotor frame (2) in Section 2.2. It reconstructs the extended Back-EMF components on estimated γ-δ axes and calculates θ_e from their orientation.

Rearranging (2) for current dynamic and applying same transformation to obtain (5) yields the voltage equations in estimated frame

$$\begin{bmatrix} v_\gamma \\ v_\delta \end{bmatrix} = \begin{bmatrix} R_s + sL_d & -\hat{\omega}_e L_q \\ \hat{\omega}_e L_q & R_s + sL_d \end{bmatrix} \begin{bmatrix} i_\gamma \\ i_\delta \end{bmatrix} + \begin{bmatrix} e_\gamma \\ e_\delta \end{bmatrix}, \tag{16}$$

where $\hat{\omega}_e$ is the speed estimation that produced by observer and (v_γ, v_δ) and (i_γ, i_δ) are measurable quantities from sensors. Solving (16) for extended Back-EMF components gives

$$\begin{aligned} \hat{e}_\gamma &= v_\gamma - R_s i_\gamma - L_d \, s \, i_\gamma + \hat{\omega}_e L_q i_\delta, \\ \hat{e}_\delta &= v_\delta - R_s i_\delta - L_d \, s \, i_\delta - \hat{\omega}_e L_q i_\gamma. \end{aligned} \tag{17}$$

Direct implementation of (17) is not practical because pure differentiator s amplifies measurement noise on currents. Two filtering stages are necessary in there. Firstly, low-pass filter is applied on each component

$$\tilde{s}\, i = \frac{\omega_c \, s}{s + \omega_c} \, i, \tag{18}$$

where ω_c is chosen well above the fundamental but below the switching harmonics. That limits band of di/dt. Secondly, to suppress the slow drift and DC bias that accumulate in (17), a high-pass filter (HPF) with the same cutoff is applied on each component

$$H_{HP}(s) = \frac{s}{s + \omega_c}. \tag{19}$$

The combined LPF and HPF structure keeps speed proportional term of E_{ex} as original, while rejecting current noise and steady-state offsets.

Once $\hat{e}_\gamma$ and $\hat{e}_\delta$ have been calculated, the estimation error is determined from their orientation with arctangent expression

$$\varepsilon_{bemf} = \text{atan2}\left(-\hat{e}_\gamma, \hat{e}_\delta\right) \approx \Delta\theta, \tag{20}$$

that takes advantage of projection structure of (5). When $\Delta\theta$ is small, the arctangent reduces to the linear approximation $\Delta\theta \approx -e_\gamma / E_{ex}$ used in Section 2.2. However, (20) preserves the correct sign and range over the full $[-\pi, \pi]$ interval. That is critical during transients where $\Delta\theta$ may briefly exceed the small angle range.

As in Section 3.1, a type-2 PLL is used to get ε_{bemf}. PI controller in this PLL drives it to zero and output of controller yields the speed estimate $\hat{\omega}_e^{bemf}$. To reduce ripple and switching noise on $\hat{\theta}_e^{bemf}$, a first-order filter is applied to the angle output with cutoff ω_{pf},

$$H_{pf}(s) = \frac{\omega_{pf}}{s + \omega_{pf}}, \tag{21}$$

As ω_e decreases, the signal-to-noise ratio of (17) changes because $\hat{e}_\gamma$ and $\hat{e}_\delta$ become smaller while measurement and quantization noise remain the same. Below the threshold mechanical speed, arctangent expression in (20) begins to lose its accuracy. Therefore, observer is enabled only above this speed threshold.

3.3. Weighted Transition Between Estimation Methods

The HFSI and Back-EMF estimations only cover their operating range, so a continuous transition between methods is required for full speed range operation. The approach applies linear speed-dependent weight with vectorial combination of the two angle estimations.

Let $\omega_1 < \omega_2$ bound transition band in electrical speed. The weighting coefficient is defined as

$$w(|\hat{\omega}_e|) = \begin{cases} 0, & |\hat{\omega}_e| < \omega_1, \\ \frac{|\hat{\omega}_e| - \omega_1}{\omega_2 - \omega_1}, & \omega_1 \le |\hat{\omega}_e| \le \omega_2, \\ 1, & |\hat{\omega}_e| > \omega_2, \end{cases} \tag{22}$$

so that $w = 0$ selects HFSI estimation, $w = 1$ selects the Back-EMF estimation, and intermediate values produce combined estimation according to weighting coefficient.

A direct combination of the two angle outputs is unsuitable because of 2π wrapping. Two estimations can differ by approximately 2π even when both are accurate. Also, when the speed exits the transition region, angle estimation would cause jump on estimation. Therefore, angle combination is performed with Cosine–Sine decomposition,

$$\begin{bmatrix} \cos\hat{\theta}_e \\ \sin\hat{\theta}_e \end{bmatrix} = (1 - w)\begin{bmatrix} \cos\hat{\theta}_e^{hf} \\ \sin\hat{\theta}_e^{hf} \end{bmatrix} + w\begin{bmatrix} \cos\hat{\theta}_e^{bemf} \\ \sin\hat{\theta}_e^{bemf} \end{bmatrix}, \tag{23}$$

from which the composite angle is recovered as

$$\hat{\theta}_e = \text{atan2}\left(\sin\hat{\theta}_e, \cos\hat{\theta}_e\right). \tag{24}$$

Interpolation is performed on unit circle instead of unwrapped angle. As a result, continuity across 2π is ensured and angle jumps are avoided.

Applied low-pass filter and rate limiter further smooth the transition. That filter applied to $|\hat{\omega}_e|$ suppresses high-frequency speed changes to prevent chattering near region limits. Also, rate limiter limits slew rate during abrupt speed transients. The resulting weighting profile and operating regimes are summarized in Figure 3.

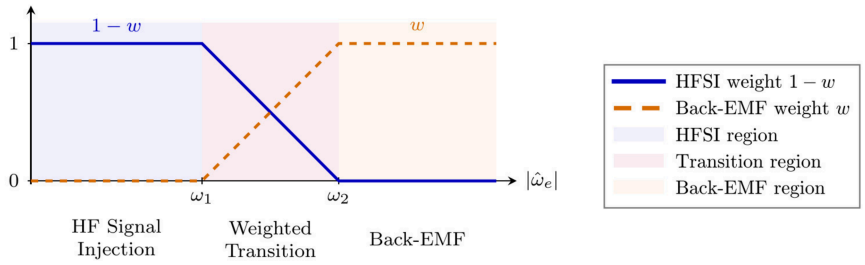


Figure 3. Speed-dependent weighting profile of the hybrid sensorless estimator.

4. Fault Detection and Control Reconfiguration

The fault detection and isolation (FDI) layer runs in parallel with the sensored FOC to generate fault flag. The hybrid estimator in (Section 3) operates continuously in the background, so residual is available across the full speed range including standstill.

4.1. Residual Generation

The residual is angular difference between encoder angle θ_{enc} and sensorless estimation $\hat{\theta}_e$ from (24). Direct subtraction is discontinuous at 2π boundary, so shortest path form

$$r = \text{atan2}\left(\sin\left(\theta_{enc} - \hat{\theta}_e\right), \cos\left(\theta_{enc} - \hat{\theta}_e\right)\right) \tag{25}$$

maps the result into $(-\pi, \pi]$ and prevents 2π wrapping issue. A washout high-pass filter removes accumulated bias between two estimations during normal operation.

4.2. Adaptive Threshold with Dynamic Scaling

A fixed threshold must exceed the worst-case transient excursion of r during speed ramps, which delays detection of low-amplitude faults [7]. The threshold is therefore formed as

$$\delta_{th} = [(1 - w)\delta_{hf} + w\delta_{be}] + k_{dyn}|i_q| \tag{26}$$

The bracketed term is the base threshold, which is not constant but is calculated according to the same speed-dependent weight coefficient described in Section 3. Here, δ_{hf} and δ_{be} are the constant threshold values associated with the HFSI and Back-EMF methods. The base threshold is interpolated between them so that each method has its own threshold. The dynamic term k_{dyn} then scales the total threshold with the q-axis current. During acceleration, large $|i_q|$ increases total threshold and suppresses false alarms. At steady state it becomes close to base threshold and sharpens sensitivity. An asymmetric rate limiter extends the decay tail so the threshold does not fade faster than the transient it tracks [8].

4.3. Fault Confirmation and Seamless Reconfiguration

When $|r| \geq \delta_{th}$, an on-delay timer requires fault to persist for T_{conf} continuously before raising fault flag. Thus, it detects fast position jumps by rejecting noise-induced faults [14]. Upon confirmation, SR latch sets the permanent fault flag F with no reset path. Reconfiguration is irreversible to avoid mode oscillation due to intermittent sensor faults [1]. The complete signal flow, from residual generation to reconfiguration, is shown in Figure 4: when the flag F is set, sensor feedback θ_{enc} is switched with hybrid sensorless estimation $\hat{\theta}_e$, reducing reconfiguration to a single position source selection. Since the estimator has been running in the background during sensored operation, $\hat{\theta}_e$ has already converged to θ_{enc}, so no transient torque is observed during transition [15].

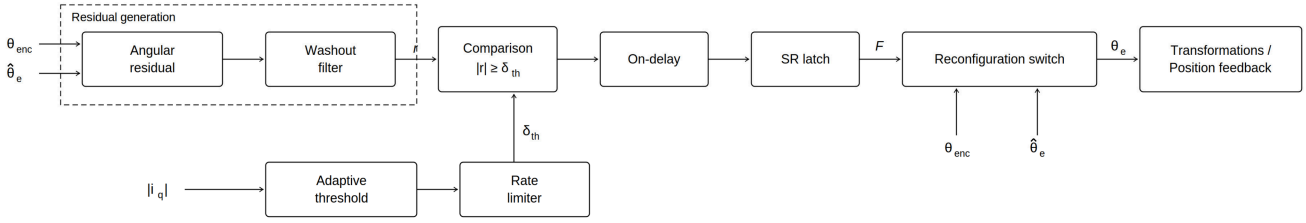


Figure 4. Signal flow diagram of the FDI and control reconfiguration; fault flag F switches angle.

5. Simulation Results and Discussion

5.1. Simulation Platform

The motor speed reference follows step ramp profile from standstill to the maximum operating speed. This speed reference is designed to pass through the HFSI-dominant region, the transition band, and the Back-EMF-dominant region. One fault-free scenario and three fault scenarios are evaluated. Fault injection is a step angle offset applied to encoder output at specified time step. The simulation platform and system parameters are listed in Table 1.

Table 1. Simulation platform and system parameters.

Parameter	Value	Parameter	Value
Motor Parameters			
R_s	0.2 Ω	ψ_m	0.2078 Wb
L_d	4.3 mH	p	3
L_q	8.7 mH	J	0.017 kg·m^2
Simulation Platform			
V_{dc}	400 V	T_s	1 µs
Estimator Parameters			
$\omega_h/2\pi$	1000 Hz	HFSI PLL	$K_p = 4$, $K_i = 100$
V_h	27 V	Back-EMF PLL	$K_p = 50$, $K_i = 2500$
Limits			
Transition band	40–60 rad/s	EMF Activation speed	15 rad/s

5.2. Steady-State Estimation Accuracy

Figure 5 shows hybrid estimator speed output ω_{est} tracking encoder speed ω_{enc} in the fault-free scenario, together with estimation error $\Delta\omega_m$ between sensor speed information and speed estimation. The hybrid output follows the reference at all three steady-state speeds with the remaining error within a narrow band. This confirms that the vectorial combination introduces no bias at any operating point.

Figure 6 zooms into the HFSI-dominant low-speed region and the Back-EMF-dominant high-speed region, comparing each estimation method against the extended Kalman filter (EKF) benchmark [16]. The saliency-based estimation $\omega_{est,inj}$ closely follows ω_{enc} at low speed, while the Back-EMF estimation $\omega_{est,emf}$ converges to the encoder reference at high speed. At low speed, EKF produces larger transient deviations, because Back-EMF amplitude decreases as electrical angular velocity approaches zero, reducing observability. At high speed, both methods converge to the reference but filter group delay and saliency mismatch in EKF model cause slight steady-state bias in EKF estimation. These findings

confirm that neither a single Back-EMF observer nor an EKF covers both regimes, motivating the hybrid architecture.

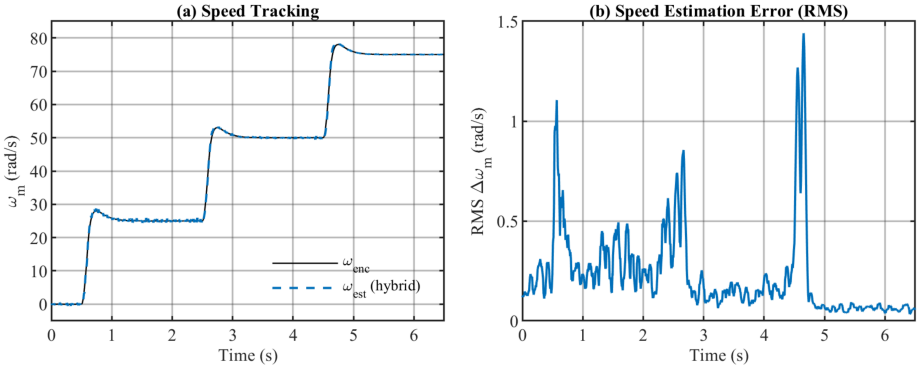


Figure 5. Fault-free scenario. (**a**) Encoder speed ω_{enc} and hybrid estimate ω_{est} over full speed range. (**b**) Estimation error $\Delta\omega_m$.

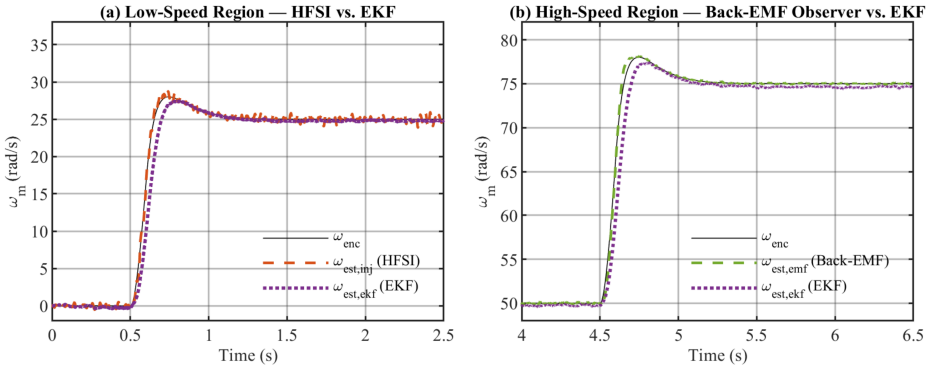


Figure 6. EKF benchmark comparison. (**a**) Low-speed region: HFSI estimate $\omega_{est,inj}$ vs. EKF estimate $\omega_{est,ekf}$. (**b**) High-speed region: Back-EMF estimate $\omega_{est,emf}$ vs. EKF estimate $\omega_{est,ekf}$.

5.3. Transient Performance During Speed Ramp

Figure 7 shows the evolution of the weighting factor w_{inj} and w_{emf} during the ramp scenario. Below the transition band $w_{inj} = 1$ and $w_{emf} = 0$, so the HFSI estimation is dominant. As the speed information enters the transition region, both weighting factors vary continuously, and the vectorial cross-fade interpolates between two estimations. Above the upper boundary $w_{inj} = 0$ and $w_{emf} = 1$, transferring full authority to Back-EMF estimation.

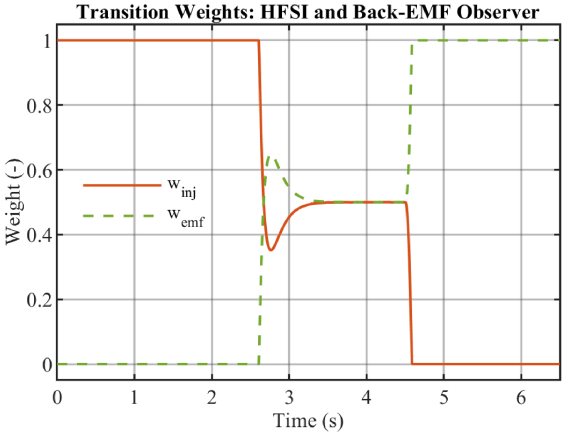


Figure 7. Weighting factor evolution during the speed ramp.

5.4. Fault Detection and Reconfiguration Response

Three fault scenarios inject a 0.5 rad step angle offset into the encoder output at different time steps, covering all three estimation regimes. In every case, the injected offset exceeds the base threshold for long enough to activate confirmation timer T_{conf}.

Scenario 1 (Figure 8) injects a fault at low speed, where HFSI estimation is dominant. The residual $r(t)$ exceeds the adaptive threshold δ_{th} immediately and remains above it for the full confirmation interval, setting the fault flag F. The speed response shows a brief transient as the controller switches to sensorless operation, with steady-state tracking recovered within one settling period.

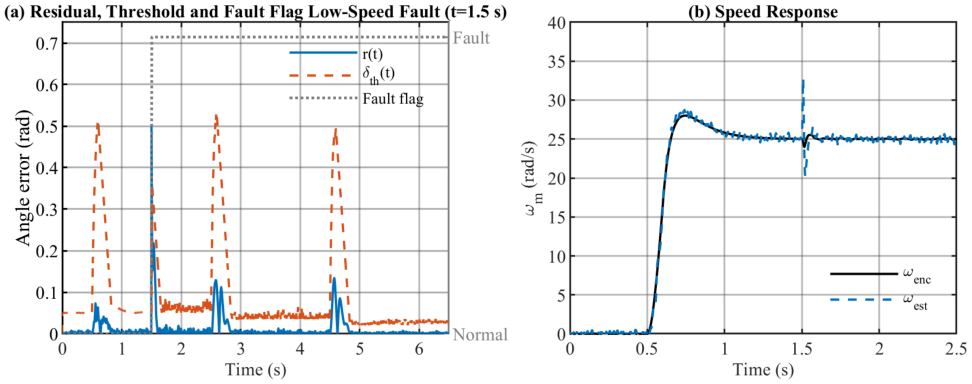


Figure 8. Scenario 1: fault injected at low speed (HFSI dominant). (**a**) Residual $r(t)$, adaptive threshold δ_{th} and fault flag F. (**b**) Speed response.

Scenario 2 (Figure 9) injects a fault in the transition region, where both estimators contribute to the combined output. The base threshold is interpolated between HFSI and Back-EMF base threshold values. The residual still exceeds the threshold cleanly, the fault flag is set within one confirmation interval, and reconfiguration speed transient is of comparable magnitude to Scenario 1.

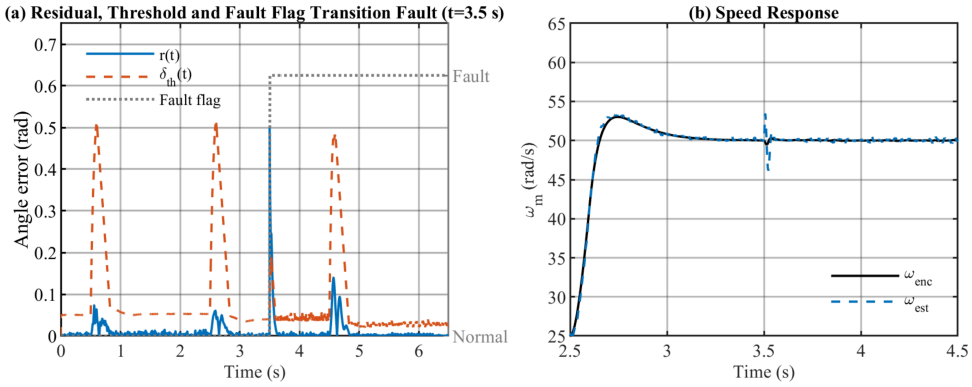


Figure 9. Scenario 2: fault injected in the transition region. (**a**) Residual $r(t)$, adaptive threshold δ_{th} and fault flag F. (**b**) Speed response.

Scenario 3 (Figure 10) injects a fault at high speed, where Back-EMF estimation is in full control. The residual clearly exceeds the adaptive threshold, the fault flag is set, and the drive continues at the same speed reference using the Back-EMF estimation, with only a minor transient response. Across all three scenarios, FDI layer produces no false alarms and achieves detection within expected confirmation time.

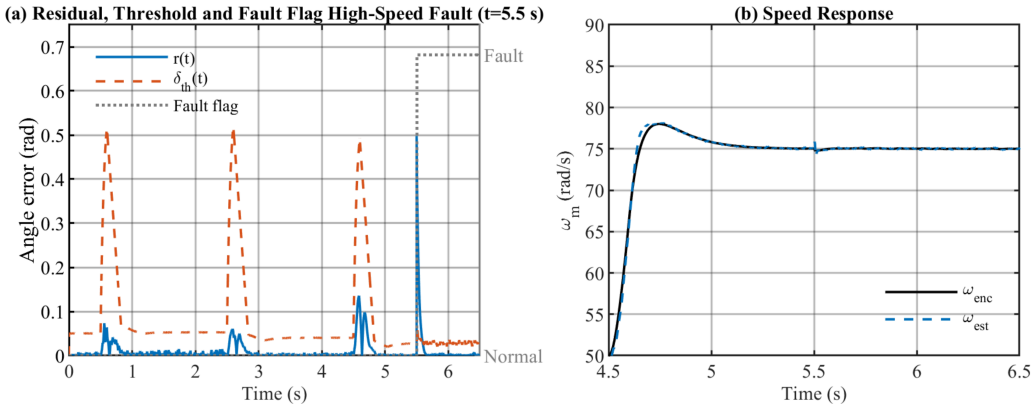


Figure 10. Scenario 3: fault injected at high speed (Back-EMF dominant). (**a**) Residual $r(t)$, adaptive threshold δ_{th} and fault flag F. (**b**) Speed response.

6. Conclusions

A position sensor fault-tolerant control architecture for IPMSM drives was developed by combining high-frequency signal injection at standstill and low speeds with an extended Back-EMF observer at medium and high speeds. These methods are combined with a vectorial weighted transition that produces a continuous rotor angle across the full speed range. A fault detection and isolation layer monitors the residual from the difference between the encoder angle and the hybrid estimation. This triggers an irreversible reconfiguration to sensorless operation with a dynamically scaled threshold and a confirmation delay at the moment of detection. Across fault scenarios, including the HFSI-dominant, transition, and Back-EMF-dominant regimes, the residual cleanly exceeds the adaptive threshold with no false alarms during speed transients and tracking recovers after reconfiguration. A comparison with the extended Kalman filter, which loses Back-EMF observability near standstill and retains a small steady-state bias at high speed, supports necessity of the hybrid structure rather than a single estimation method. Future work will focus on extending structure to multiple parallel sensor faults and performing experimental validation on a hardware test bench.

Author Contributions: Conceptualization, B.S. and F.C.; methodology, B.S.; software, B.S.; validation, B.S.; formal analysis, B.S.; investigation, B.S.; writing—original draft preparation, B.S.; writing—review and editing, B.S. and F.C.; visualization, B.S.; supervision, F.C.; project administration, F.C. All authors have read and agreed to the published version of the manuscript.

Funding: This research received no external funding.

Institutional Review Board Statement: Not applicable

Informed Consent Statement: Not applicable

Data Availability Statement: The original contributions presented in this study are included in the article. Further inquiries can be directed to the corresponding author.

Conflicts of Interest: The authors declare no conflicts of interest.

Abbreviations

The following abbreviations are used in this manuscript:

Back-EMF	Back-Electromotive Force
CUSUM	Cumulative Sum
EKF	Extended Kalman Filter
FDI	Fault Detection and Isolation

FOC	Field-Oriented Control
FTC	Fault-Tolerant Control
HF	High-Frequency
HFSI	High-Frequency Signal Injection
HPF	High-Pass Filter
IPMSM	Interior Permanent Magnet Synchronous Motor
LPF	Low-Pass Filter
PI	Proportional–Integral
PLL	Phase-Locked Loop
PMSM	Permanent Magnet Synchronous Motor

References

1. Jeong, Y.-S.; Sul, S.-K.; Schulz, S.E.; Patel, N.R. Fault detection and fault-tolerant control of interior permanent-magnet motor drive system for electric vehicle. *IEEE Trans. Ind. Appl.* **2005**, *41*, 46–51. [CrossRef]
2. Meinguet, F.; Kestelyn, X.; Semail, E.; Gyselinck, J. Fault detection, isolation and control reconfiguration of three-phase PMSM drives. In Proceedings of the IEEE International Symposium on Industrial Electronics (ISIE) 2011, Gdańsk, Poland, 27–30 June 2011; pp. 2091–2096.
3. Morimoto, S.; Kawamoto, K.; Sanada, M.; Takeda, Y. Sensorless control strategy for salient-pole PMSM based on extended EMF in rotating reference frame. *IEEE Trans. Ind. Appl.* **2002**, *38*, 1054–1061. [CrossRef]
4. Liu, J.M.; Zhu, Z.Q. Novel sensorless control strategy with injection of high-frequency pulsating carrier signal into stationary reference frame. *IEEE Trans. Ind. Appl.* **2014**, *50*, 2574–2583. [CrossRef]
5. Luo, X.; Tang, Q.; Shen, A.; Zhang, Q. PMSM sensorless control by injecting HF pulsating carrier signal into estimated fixed-frequency rotating reference frame. *IEEE Trans. Ind. Electron.* **2016**, *63*, 2294–2303. [CrossRef]
6. Wu, X.; Wu, T.; Huang, S.; Pan, W.; Lyu, M.; He, Y.; Cui, H. Hybrid position estimation strategy with a smooth transition for IPMSM sensorless drives in the wide speed range. *IEEE Trans. Power Electron.* **2022**, *37*, 7916–7930. [CrossRef]
7. Lee, D.; Akatsu, K. An improved position sensor fault detection and algorithm transition using adaptive threshold for sensorless control of IPMSM. In Proceedings of the IEEE Energy Conversion Congress and Exposition (ECCE) 2019, Baltimore, MD, USA, 29 September–3 October 2019; pp. 910–915.
8. Lee, D.; Akatsu, K. The study on sensor fault detection and algorithm transition using adaptive threshold in position self-sensing control for IPMSM. *IEEE Trans. Ind. Electron.* **2021**, *68*, 10459–10469. [CrossRef]
9. Taege, S.; Schiefhauer, H.; Ali, A.; Müller, B.; Janek, G. Simple fault-tolerant control of a permanent magnet synchronous motor with faulty position sensor. In Proceedings of the IEEE International Electric Machines and Drives Conference (IEMDC) 2023, San Francisco, CA, USA, 15–18 May 2023; pp. 1–10.
10. Gao, G.; Zhong, Y.; Gao, S.; Gao, B. Double-Channel Sequential Probability Ratio Test for Failure Detection in Multisensor Integrated Systems. *IEEE Trans. Instrum. Meas.* **2021**, *70*, 3514814. [CrossRef]
11. Gao, B.; Hu, G.; Zhu, X.; Zhong, Y. A Robust Cubature Kalman Filter with Abnormal Observations Identification Using the Mahalanobis Distance Criterion for Vehicular INS/GNSS Integration. *Sensors* **2019**, *19*, 5149. [CrossRef] [PubMed]
12. Chen, J.; Wang, B.; Li, S.; Cheng, Y.; Chen, J.; Dong, H. Fault Diagnosis and Fault-Tolerant Control of Permanent Magnet Synchronous Motor Position Sensors Based on the Cubature Kalman Filter. *Sensors* **2025**, *25*, 6030. [CrossRef] [PubMed]
13. Ichikawa, S.; Chen, Z.; Tomita, M.; Doki, S.; Okuma, S. Sensorless control of an interior permanent magnet synchronous motor on the rotating coordinate using an extended electromotive force. In Proceedings of the 27th Annual Conference of the IEEE Industrial Electronics Society (IECON) 2001, Denver, CO, USA, 29 November–2 December 2001; pp. 1667–1672.
14. Lee, D.; Akatsu, K. The study on position sensor fault detection and algorithm transition from sensored to sensorless control for IPMSM. In Proceedings of the IEEE 12th International Conference on Power Electronics and Drive Systems (PEDS) 2017, Honolulu, HI, USA, 12–15 December 2017; pp. 728–733.
15. Lee, T.; Lee, H.; Jang, P.; Hwang, Y.; Nam, K. Position fault detection for UAM motor with seamless transition. *IEEE Access* **2021**, *9*, 168042–168054. [CrossRef]
16. Mwasilu, F.; Jung, J.-W. Enhanced fault-tolerant control of interior PMSMs based on an adaptive EKF for EV traction applications. *IEEE Trans. Power Electron.* **2016**, *31*, 5746–5758. [CrossRef]

Disclaimer/Publisher's Note: The statements, opinions and data contained in all publications are solely those of the individual author(s) and contributor(s) and not of MDPI and/or the editor(s). MDPI and/or the editor(s) disclaim responsibility for any injury to people or property resulting from any ideas, methods, instructions or products referred to in the content.